LETTER

Design and simulation of a neural interface based on a microfluidic flexible interconnection cable for chemical delivery

Yoo Na Kang[1*] , Jun-Uk Chu[1], Kang-Ho Lee[1], Yongkoo Lee[1] and Sohee Kim[2]

Abstract

Neural interfaces are fundamental tools for transmitting information from the nervous system. Research on the immune response of an invasive neural interface is a field that requires continuous effort. Various efforts have been made to overcome or minimize limitations through modifying the designs and materials of neural interfaces, modifying surface characteristics, and adding functions to them. In this study, we demonstrate microfluidic channels with crater-shaped structures fabricated using parylene-C membranes for fluid delivery from the perspective of theory, design, and simulation. The simulation results indicated that the fluid flow depended on the size of the outlet and the alignment of microstructures inside the fluidic channel. All the results can be used to support the design of microfluidic channels made by membranes for drug delivery.

Keywords: Neural interface, Flexible interconnection cable, Microfluidic channel, Drug delivery

Introduction

About a decade ago, massive projects to unravel the mechanism and function of the human brain started, such as the Human Brain Project, BRAIN Initiative, and Brain/MIND (Brain Mapping by Integrated Neurotechnologies for Disease Studies), and remarkable research progress has been achieved in neuroscience, medicine, and information and communications technology (ICT)-based scientific research [1–4]. Those research initiatives have also led to advances in neural interfaces, which is an essential tool for discovering the brain's mystery [5]. Non-invasive or invasive tools capable of the precise recording of neural signals have been developed [6]. Among them, invasive neural interfaces are promising tools because of their ability to collect more sophisticated and direct electrophysiological data [5]. Silicon-based invasive neural interfaces have been widely used, and their performance

has been proven in many studies [7–10]. However, long-lasting integration of invasive neural interfaces with the neural tissue is the most challenging issue to be addressed at present [11]. Various efforts have been made to overcome the immune response induced by the implantation of neural interfaces, such as modifying the designs and materials of neural interfaces, modifying surface characteristics, and adding functions to them [12, 13]. In particular, direct injection of anti-inflammatory reagents to the brain can minimize the effect of the blood–brain barrier (BBB) and blood–cerebrospinal fluid barrier (BCB) [14]. Microfluidic channels integrated with a neural interface enable precise and stable delivery of even a minimal amount of drugs for reducing immune responses or providing chemical stimulation [15]. In a previous study, we developed a microfluidic flexible interconnection cable (μFIC) that delivers a fluid to the 3D-shaped electrodes of the flexible penetrating microelectrode array (FPMA) [8]. Drug delivery through microfluidic channels is expected to improve chronic implantation reliability, as it can deliver anti-inflammatory drugs precisely to the implanted tissue.

*Correspondence: ynkang@kimm.re.kr

[1] Department of Medical Device, Korea Institute of Machinery and Materials (KIMM), Daegu 42994, Republic of Korea
Full list of author information is available at the end of the article

In this study, we investigated the effects of the design of the microfluidic channel formed inside the μFIC on the fluid velocity at the outlet of the microfluidic channel. We simulated the fluid flow according to the inlet pressure and the additional structures formed inside the microfluidic channel, depending on the size and arrangement of these additional structures.

Methodology

Simulation of microfluidic flexible interconnection cable

The most basic structure of microfluidic channels is a narrow and long passage for a fluid to flow [16]. The microfluidic channel proposed in this study was a single channel with multiple crater-shaped structures when viewed from the top, which can be described as pillars when viewed from the inside of the microfluidic channel. Figure 1a shows a schematic diagram of the μFIC integrated with a microfluidic channel inside. The microfluidic channel consisted of an inlet under the reservoir and an outlet on the side of the electrode pads. As the proposed microfluidic channel was made of two layers of thin membranes, it was difficult to maintain the shape of the channel unblocked. However, the crater-shaped structures were advantageous in maintaining the shape of the fluidic channel unblocked because these structures supported the upper layer of the channel to prevent its collapse. Figure 1b shows the top and cross-sectional views of the microfluidic channel. The actual shape of the microfluidic channel was an arch with a large radius of curvature, as shown in Fig. 1b. However, the simulation model was simplified from crater-shaped structures to circles to achieve a concise and fast result. The radius and arrangement
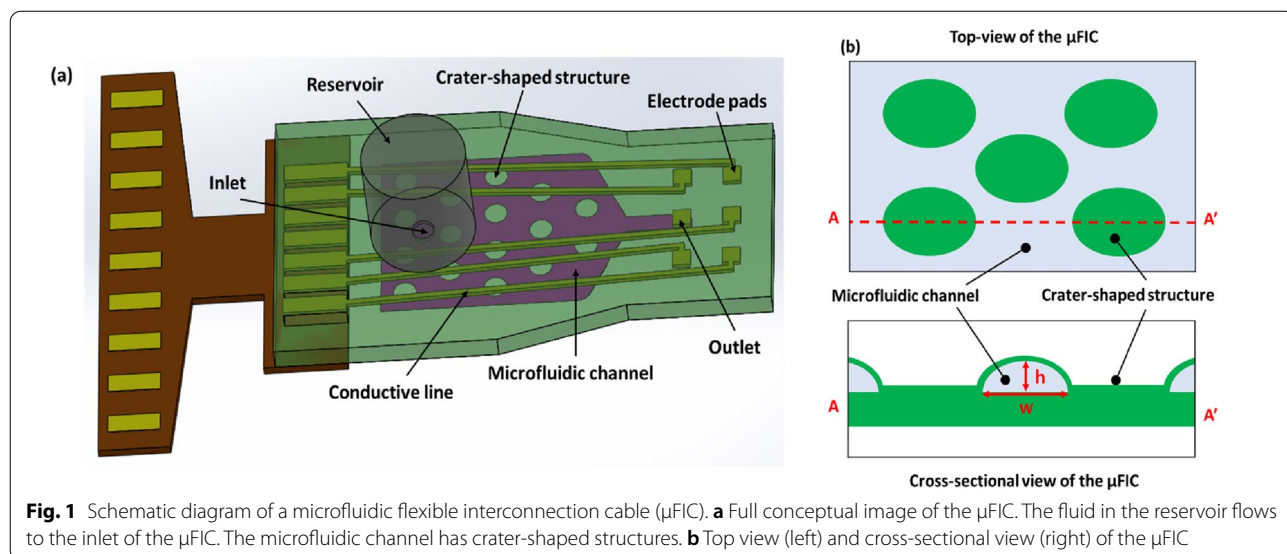
of the crater-shaped structures were considered to be essential modeling parameters of the microfluidic channel because these can regulate the volume and flow velocity of the fluid that is contained in the channel. As for alignment, the first simulation model had an inline channel, which is rows of crater-shaped structures in the microfluidic channel, while the second model had a zigzag channel, which is crater-shaped structures arranged in a staggered position.

Static analysis with laminar flow interface in COM-SOL Multiphysics® was used to simulate the flow velocity and pressure field. Two alignments with different radii of crater-shaped structures were used for the geometry of the device. The working fluid was assumed to be water for simplified simulations. The governing equations for incompressible liquid flow were the continuity equation and the Navier–Stokes equation, as shown below. Each represents the conservation of mass and momentum.

$$\rho \nabla \cdot (\mathbf{u}) = 0 \tag{1}$$

$$\nabla \cdot \left[-p\mathrm{I} + \mu(\nabla \boldsymbol{u} + (\nabla \boldsymbol{u})^T \right] + \boldsymbol{F} = \rho(\boldsymbol{u} \cdot \nabla)\boldsymbol{u} \tag{2}$$

where $\boldsymbol{u}$ is the fluid velocity vector, p is the pressure, I is the unit diagonal matrix, and $\boldsymbol{F}$ represents the volume force vector. No slip condition, that is, the fluid at the wall is not moving, was used for the boundary conditions. Also, the initial inlet pressure was assumed to be the hydrostatic pressure of the reservoir. As the reservoir was coated with a hydrophobic material (Parylene-C), the internal surface tension of the reservoir was neglected. The pressure at the outlet was set to zero.

Fig. 1 Schematic diagram of a microfluidic flexible interconnection cable (μFIC). **a** Full conceptual image of the μFIC. The fluid in the reservoir flows to the inlet of the μFIC. The microfluidic channel has crater-shaped structures. **b** Top view (left) and cross-sectional view (right) of the μFIC

Kang *et al. Micro and Nano Systems Letters*   (2022) 10:19

Page 3 of 7

## Fabrication of the microfluidic flexible interconnection cable

The microfluidic flexible interconnection cable was fabricated based on parylene-C, a biocompatible and highly flexible material. Ti as a sacrificial layer in a thickness of 200 nm and the first parylene-C layer in a thickness of 3 μm were sequentially deposited on the substrate. An adhesive layer (Cr) and conductive metal (Au) were sputtered in thickness of 25/200 nm, and then conductive lines were patterned through photolithography. The second parylene-C layer was deposited to insulate the conductive lines in a thickness of 3 μm. To fabricate the microfluidic channel, a 40 μm thick photoresist (PR, AZ®40XT, Microshemicals, UIm, Germany) was patterned on the second parylene-C layer, the final parylene-C layer was deposited in a thickness of 6 μm. The electrode pads, the inlet, and the outlet of the microfluidic channel were opened by oxygen plasma etching. Finally, μFICs were floated from the substrate by Ti etchant, and μFICs were soaked in acetone to remove the PR pattern. The microfluidic channel was formed in the space where the photoresist structures had been removed. Crater-shaped structures were formed on the concave patterns of the photoresist (Fig. 2).

Results and discussion

Analysis of fluid flow through the microfluidic channel

We assumed that the radius of the crater-shaped structures is constant to simplify the simulation. Simulations were performed on the plain channel with no crater-shaped structures as a reference and two modified fluidic channels with crater-shaped structures. The length of the channel was approximately 14 mm and the width was 3 mm. The width of the channel near the outlet was 160 μm. The radii of the outlet (r) and crater-shaped structures (R) were changed to investigate the effects of each on the fluid flow at the outlet. Three different radii (r = 0.22, 0.1, and 0.15 mm) for the outlet and six different radii (R = 0.1, 0.12, 0.14, 0.15, 0.16, and 0.18 mm) for the crater-shaped structures were simulated. The
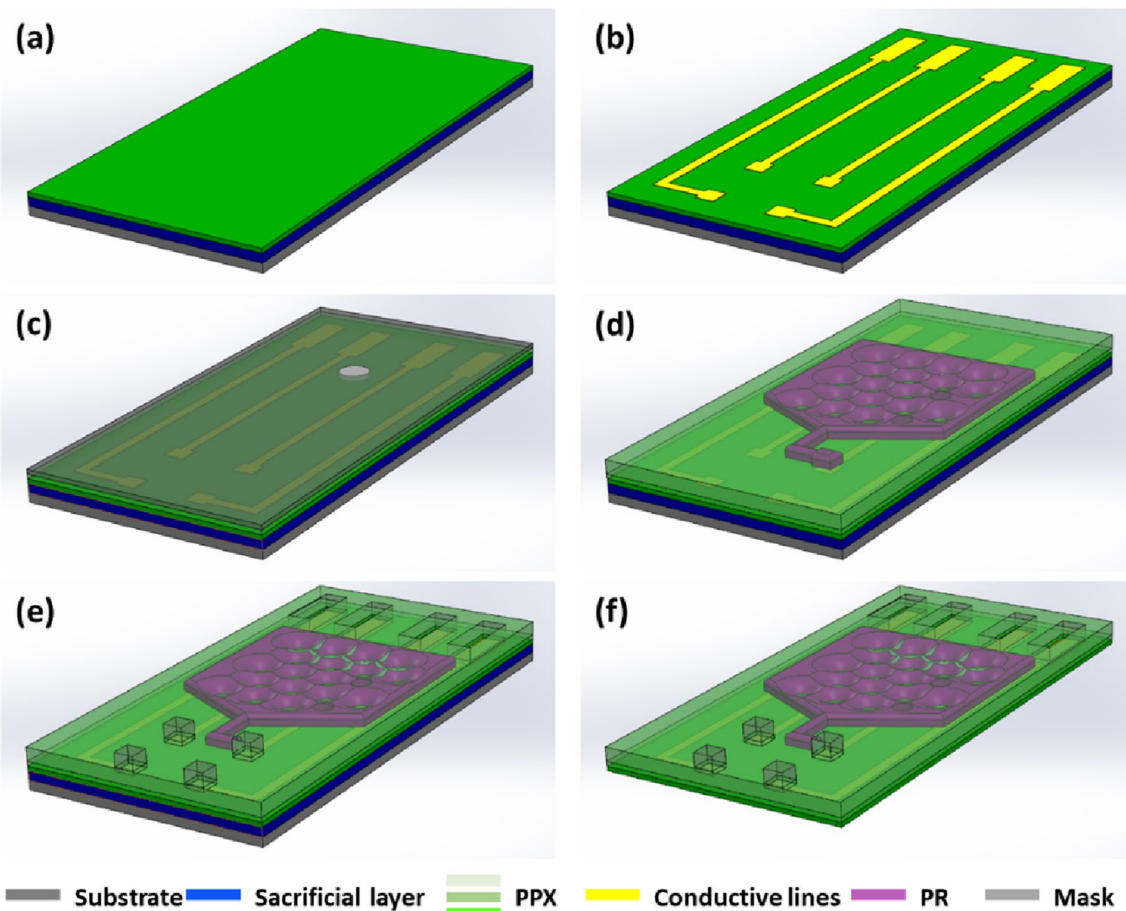
Fig. 2 Fabrication processes of a parylene-C-based μFIC. **a**–**f** MEMS techniques including sputtering, photolithography, deposition, and dry etching were used for fabrication

simulation results demonstrate that near the outlet, the pressure was relatively low and the velocity was concentrated. Figure 3 shows the representative pressure field and velocity magnitude of the microfluidic channel with r = 0.02 mm and R = 0.18 mm. In the plain channel with no pillars, the average velocity was 111.44 mm/s, and the maximum velocity near the outlet was 142.32 mm/s. The average velocity in the inline channel was 7.19 mm/s, and in the zigzag channel, it was 9.85 mm/s.

The flow rate was calculated based on the simulation results. The average flow rates in the plain channel, the inline channel, and the zigzag channel were 8.40 µL/min, 0.54 µL/min, and 0.74 µL/min, respectively. Comparing Fig. 3d, e, f, the velocity of the fluid near the outlet was clearly changed. The velocity magnitude in the zigzag channel was slightly increased due to the position of the structures. Figure 4 shows the flow rate at the outlet according to the radius of the outlet and the inner pillar structures, with a constrained size of the outlet. The initial input pressure was calculated by the dimension of the reservoir, resulting in a value of about 80 kPa, indicating a state of a filled reservoir. As the fluid in the reservoir flowed out, the input pressure was also reduced. The

flow rate of the plain channel was significantly different from that of the microfluidic channels with inner structures. Also, the results show that the flow rate was slow at the smaller outlet (Fig. 4a–c). For the outlet with radii of 0.1 mm and 0.15 mm, the results were similar. However, when the radius of the outlet was 0.02 mm, there was a big difference in the resultant flow rate. In our study, a neural interface is designed to be implanted in rodents, mainly Sprague–Dawley rats, to verify the device. The total volume of cerebrospinal fluid (CSF) in adult SD rats is about 400 µL [17]. And reproduction rate of CSF is 1.4 to 3.38 µL/min [17, 18]. The desired design values take into account the reproduction rate of CSF. The outlet radius of 0.02 mm seems too small flow rate, and 0.15 mm is too large. The outlet size of 0.1 mm is estimated as most appropriate. Moreover, the plain channel and inline channel are vulnerable to bending and folding.

Fabrication of the microfluidic flexible interconnection cable

The microfluidic flexible interconnection cable was fabricated based on the simulation results. The zigzag channel was adopted, and the radius of the outlet was 0.1 mm.
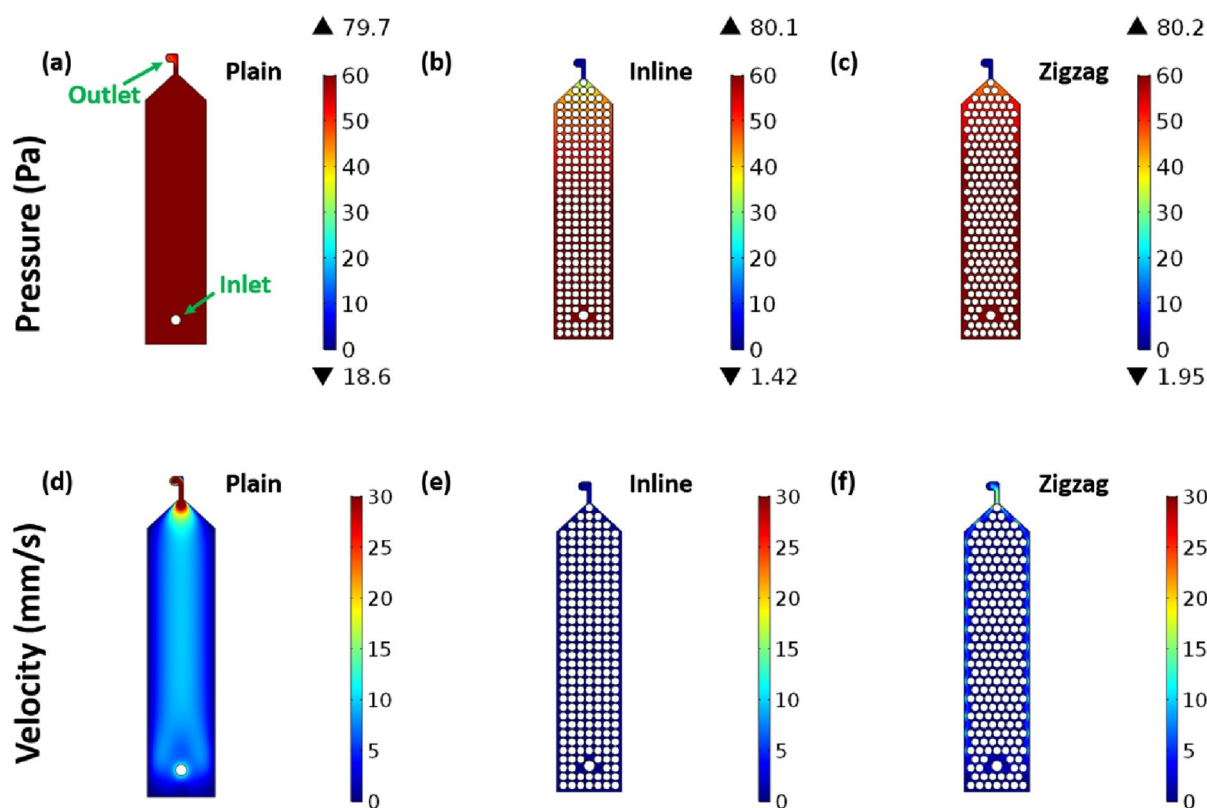
Fig. 3 Simulated results of the pressure and velocity of the fluid flow in the µFIC. **a**, **d** The pressure and velocity of the fluid flow in the microfluidic channel without inner structures. **b**, **e**) The channel with crater-shaped structures positioned inline and **c**, **f** the channel with crater-shaped structures positioned in a zigzag fashion
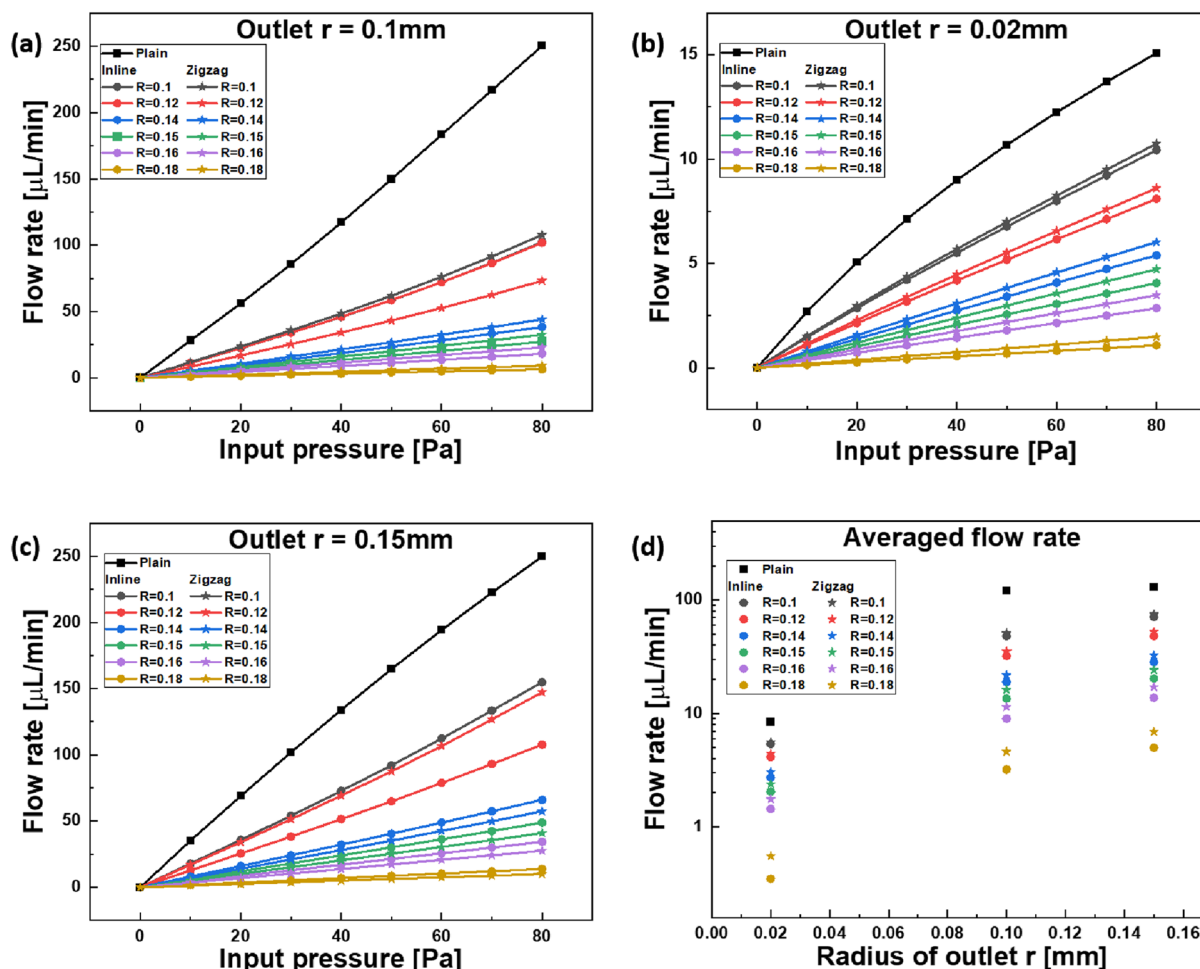
Fig. 4 Simulated results of flow rate at the outlet in microfluidic channel designs. **a**–**c** The flow rates with different radii of crater-shaped structures (R) at a fixed radius of the outlet (r). **d** The average flow rate of the fluid decreases according to the increased radius of the crater-shaped structures

The pattern and size of the outlet followed the simulation results. In the simulation, the radius of 0.18 mm of the crater-shaped structure was the best choice. The acceptable input pressure is approximately 30 Pa. However, structures with a radius of 0.1 mm were fabricated considering the contained volume of the microfluidic channel. The fabricated µFIC is shown in Fig. 5. The crater-shaped structures were formed using the PR reflow technique [19]. Figure 5 shows the optical images and scanning electron microscope (SEM) images before (Fig. 5a, b) and after the PR reflow process (Fig. 5d, e). The PR pattern was smoothed after the thermal treatment. The crater-shaped structures were formed, and then the shape was confirmed using the surface profile measurement (Fig. 5c, f). A rounded edge was considered more advantageous for membrane deposition and fluid flow than sharp edges. Figure 5g, h show the optical images of the fabricated µFIC with crater-shaped structures. The channel was fabricated by parylene-C layers so that it is transparent. Multiple conductive lines for the transmission of neural signals were located under the microfluidic channel.

Conclusions

We simulated the microfluidic flexible interconnection cable with different channel designs in terms of fluid flow characteristics using COMSOL Multiphysics®. The smaller outlet and larger inner structures tended to reduce the flow rate. The larger inner structures, however, reduced the fluid volume that can be contained in the microfluidic channel, which imposes a trade-off relation. Therefore, an appropriate design of the channel should be derived according to the application. For drug delivery to rodent brains, an acceptable flow rate range is up to 3.38 µL/min [18, 20]. The final design of the microfluidic channel was chosen to satisfy this flow

Kang *et al. Micro and Nano Systems Letters*   (2022) 10:19

Page 6 of 7
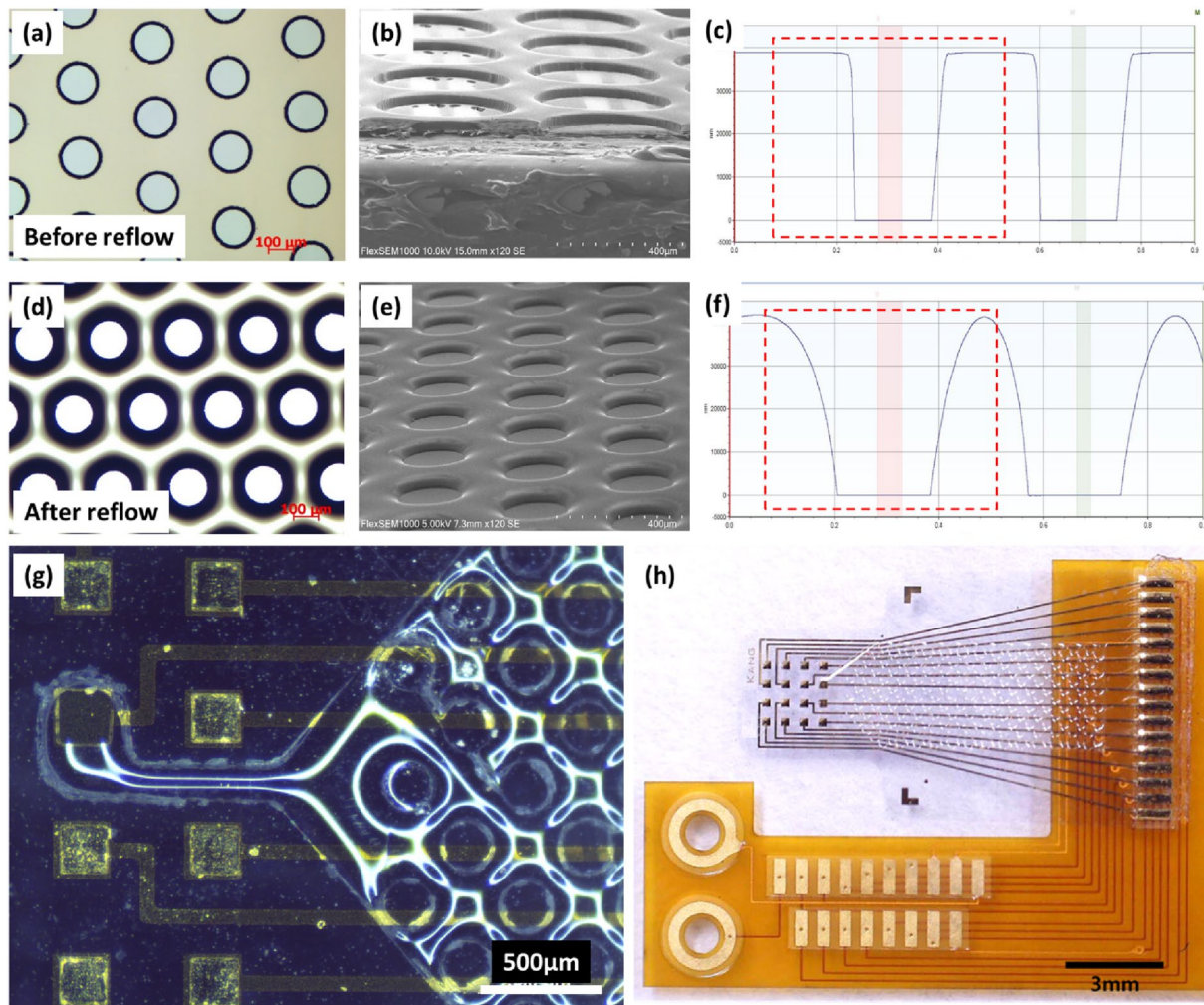
Fig. 5 Images of the crater-shaped structures and the completed µFIC. The optical images (**a**, **d**) and scanning electron microscope (SEM) images (**b**, **e**) are compared before and after PR reflow. **c**, **f** The surface profiles of PR before and after PR reflow. **g**, **h** The optical images of the fabricated µFIC with crater-shaped structures aligned in a zigzag fashion

rate, considering the volume that can be contained in the fluidic channel. Although the average velocity in the inline channel was slower than in the zigzag channel, the zigzag channel was more robust in maintaining its shape when the µFIC was bent or folded. Therefore, the zigzag channel was finally adopted and fabricated. The dimension of the outlet and the crater-shaped structure was based on the simulation results. In addition, external pressure was considered. In this study, we fabricated the microfluidic flexible interconnection cable with the outlet and crater of 0.1 mm radius and the crater-shaped structures with a radius of 0.1 mm. The device was fabricated with a larger flow rate than the simulation result because of considering the external pressure in the brain. The simulated data and the fabricated

µFIC are expected to be valuable tools for drug delivery to neural interfacing devices. Based on the result of this study, anti-inflammatory drugs are expected to be delivered effectively, and as a result, drug delivery by microfluidic flexible interconnection cable would contribute to extending the lifespan of implantable neural interfaces.

Authors' contributions
Conceptualization: YNK, SK; Methodology: YNK, JUC, KHL, YL; Investigation and formal analysis: YNK; Validation: YNK, JUC, KHL, YL, SK; Resources: YNK, SK; Visualization: YNK; Writing—original draft: YNK; Writing—review and editing: YNK, SK. All authors read and approved the final manuscript.

Availability of data and materials
The datasets used and/or analyzed during the current study are available from the corresponding author on reasonable request.

Declarations

Ethics approval and consent to participate
Not applicable.

Consent for publication
Not applicable.

Competing interests
The authors declare that they have no known competing financial interests or personal relationships that could have appeared to influence the work reported in this paper.

Author details
[1]Department of Medical Device, Korea Institute of Machinery and Materials (KIMM), Daegu 42994, Republic of Korea. [2]Department of Robotics and Mechatronics Engineering, Daegu Gyeongbuk Institute of Science and Technology (DGIST), Daegu 42988, Republic of Korea.

References

1. Insel TR, Landis SC, Collins FS (2013) The NIH BRAIN initiative. Science 340(6133):687–688. https://doi.org/10.1126/science.1239276
2. Schwartz A (2013) First volley in the brain race? Ann Neurol 73(6):A7. https://doi.org/10.1002/ana.23957
3. Grillner S, Ip N, Koch C, Koroshetz W, Okano H, Polachek M et al (2016) Worldwide initiatives to advance brain research. Nat Neurosci 19(9):1118–1122. https://doi.org/10.1038/nn.4371
4. Sim JY, Haney MP, Park SI, McCall JG, Jeong JW (2017) Microfluidic neural probes: in vivo tools for advancing neuroscience. Lab Chip 17(8):1406–1435. https://doi.org/10.1039/C7LC00103G
5. Fekete Z (2015) Recent advances in silicon-based neural microelectrodes and microsystems: a review. Sens Actuators B Chem 215:300–315. https://doi.org/10.1016/j.snb.2015.03.055
6. Gu C, Jiang J, Tao TH, Wei X, Sun L (2021) Long-term flexible penetrating neural interfaces: materials, structures, and implantation. Science China Inf Sci 64(12):1–18. https://doi.org/10.1007/s11432-021-3321-7
7. Lopez CM, Andrei A, Mitra S, Welkenhuysen M, Eberle W, Bartic C et al (2014) An implantable 455-active-electrode 52-channel CMOS neural probe. IEEE J Solid State Circuits 49(1):248–261. https://doi.org/10.1109/JSSC.2013.2284347
8. Kang YN, Chou N, Jang J-W, Choe HK, Kim S (2021) A 3D flexible neural interface based on a microfluidic interconnection cable capable of chemical delivery. Microsyst Nanoeng 7(1):66. https://doi.org/10.1038/s41378-021-00295-6
9. Chou N, Shin H, Kim K, Chae U, Jang M, Jeong U-J et al (2022) A multimodal multi-shank fluorescence neural probe for cell-type-specific electrophysiology in multiple regions across a neural circuit. Adv Sci 9(2):2103564. https://doi.org/10.1002/advs.202103564
10. Chae U, Shin H, Choi N, Ji M-J, Park H-M, Lee SH et al (2021) Bimodal neural probe for highly co-localized chemical and electrical monitoring of neural activities in vivo. Biosens Bioelectron 191:113473. https://doi.org/10.1016/j.bios.2021.113473
11. Otte E, Vlachos A, Asplund M (2022) Engineering strategies towards overcoming bleeding and glial scar formation around neural probes. Cell Tissue Res 387(3):461–477. https://doi.org/10.1007/s00441-021-03567-9
12. Wunderlich H, Kozielski KL (2021) Next generation material interfaces for neural engineering. Curr Opin Biotechnol 72:29–38. https://doi.org/10.1016/j.copbio.2021.09.005
13. Gori M, Vadalà G, Giannitelli SM, Denaro V, Di Pino G (2021) Biomedical and tissue engineering strategies to control foreign body reaction to invasive neural electrodes. Front Bioeng Biotechnol 9:659033. https://doi.org/10.3389/fbioe.2021.659033
14. Kaurav H, Kapoor DN (2017) Implantable systems for drug delivery to the brain. Ther Deliv 8(12):1097–1107. https://doi.org/10.4155/tde-2017-0082
15. Mancera-Andrade EI, Parsaeimehr A, Arevalo-Gallegos A, Ascencio-Favela G, Parra-Saldivar R (2018) Microfluidics technology for drug delivery: a review. Front Biosci Elite 10(1):74–91. https://doi.org/10.2741/e809
16. Chen Z, Memon K, Cao Y, Zhao G (2020) A microfluidic approach for synchronous and nondestructive study of the permeability of multiple oocytes. Microsyst Nanoeng 6(1):55. https://doi.org/10.1038/s41378-020-0160-4
17. Janson J, Andersson G, Bergquist L, Eriksson M, Folgering JHA (2020) Impact of chemical modification of sulfamidase on distribution to brain interstitial fluid and to CSF after an intravenous administration in awake, freely-moving rats. Mol Genet Metab Rep 22:100554. https://doi.org/10.1016/j.ymgmr.2019.100554
18. Chodobski A, Szmydynger-Chodobska J, Johanson CE (1998) Vasopressin mediates the inhibitory effect of central angiotensin II on cerebrospinal fluid formation. Eur J Pharmacol 347(2):205–209. https://doi.org/10.1016/S0014-2999(98)00229-5
19. Porkolab GA, Apiratikul P, Wang B, Guo SH, Richardson CJK (2014) Low propagation loss AlGaAs waveguides fabricated with plasma-assisted photoresist reflow. Opt Express 22(7):7733–7743. https://doi.org/10.1364/OE.22.007733
20. Liu G, Mestre H, Sweeney AM, Sun Q, Weikop P, Du T et al (2020) Direct measurement of cerebrospinal fluid production in mice. Cell Rep 33(12):108524. https://doi.org/10.1016/j.celrep.2020.108524

Publisher's Note